Mon. Not. R. Astron. Soc. **000**, 1–15 (2014) Printed 11 November 2014 (MN LATEX style file v2.2)

Matched filter optimization of kSZ measurements with a reconstructed cosmological flow field.

Ming Li[1,2⋆], R. E. Angulo[3], S. D. M. White[2], J. Jasche[4]
[1]*Purple Mountain Observatory, West Beijing Rd. 2, 210008 Nanjing, People's Republic of China.*
[2]*Max-Planck-Institute for Astrophysics, Karl-Schwarzschild-Str. 1, D-85740 Garching, Germany.*
[3]*Centro de Estudios de Física del Cosmos de Aragón, Plaza San Juan 1, Planta-2, 44001, Teruel, Spain.*
[4]*Institut d'Astrophysique de Paris (IAP), UMR 7095, CNRS - UPMC Université Paris 6, 98bis boulevard Arago, F-75014 Paris, France.*

arXiv:1404.0007v2 [astro-ph.CO] 10 Nov 2014

11 November 2014

ABSTRACT

We develop and test a new statistical method to measure the kinematic Sunyaev-Zel'dovich (kSZ) effect. A sample of independently detected clusters is combined with the cosmic flow field predicted from a galaxy redshift survey in order to derive a matched filter that optimally weights the kSZ signal for the sample as a whole given the noise involved in the problem. We apply this formalism to realistic mock microwave skies based on cosmological N-body simulations, and demonstrate its robustness and performance. In particular, we carefully assess the various sources of uncertainty, cosmic microwave background primary fluctuations, instrumental noise, uncertainties in the determination of the velocity field, and effects introduced by miscentring of clusters and by uncertainties of the mass-observable relation (normalization and scatter). We show that available data (*Planck* maps and the MaxBCG catalogue) should deliver a 7.7σ detection of the kSZ. A similar cluster catalogue with broader sky coverage should increase the detection significance to $\sim 13\sigma$. We point out that such measurements could be binned in order to study the properties of the cosmic gas and velocity fields, or combined into a single measurement to constrain cosmological parameters or deviations of the law of gravity from General Relativity.

Key words: methods: statistical – cosmic background radiation – cosmology: theory – large-scale structure of Universe.

1 INTRODUCTION

The cosmic microwave background (CMB) radiation has a prime role in modern cosmology. Its study not only gives us access to early-Universe physics and to tight constraints on the parameters of the background cosmological model, but also allows us to explore the properties of baryons and dark matter (DM) in the low-redshift Universe. The pioneering exploration of the CMB was carried out by the *Cosmic Background Explorer* (*COBE*) satellite which provided the first detection of temperature fluctuations. More recently, the *Wilkinson Microwave Anisotropy Probe* (*WMAP*) and *Planck* satellites have provided ever more detailed and accurate full-sky CMB anisotropy maps, which have even been able to detect lensing of the CMB photons by the large-scale structure of the Universe.

The structure in the CMB radiation can be classified into two types. 'Primary anisotropies' are those resulting from physics before or on the last scattering surface, whereas 'secondary anisotropies' are those caused by the interaction of CMB photons with intervening structures at lower redshift. Among the latter, the Sunyaev-Zel'dovich effects (SZ; Sunyaev & Zeldovich 1972, 1980a,b) are particularly important and interesting.

The SZ effects refer to the inverse Compton scattering of CMB photons by free electrons in the hot intracluster and intergalactic gas that they encounter on their journey from $z \sim 1100$ to $z = 0$. This scattering results in a net energy gain of CMB photons at fixed number density and consequently distorts their spectrum. This effect is known as the thermal SZ effect (hereafter tSZ). Motions of the plasma with respect to the CMB rest frame produces Doppler effects which shift the temperature of the CMB spectrum while maintaining its blackbody form. This is known as the kinematic SZ effect (hereafter kSZ). The tSZ and kSZ imprint characteristic patterns in the CMB sky, which reflect the structure of the intergalactic gas at (relatively) low redshifts, so by identifying these patters, we can learn about the distribution of the baryons at the corresponding epochs.

The tSZ effect provides a measurement of the integral of the electron pressure along each line-of-sight to the recombination surface. The signals detected so far have primarily been due to the hot and dense gas in the intracluster medium of intervening galaxy groups and clusters. The kSZ, on the other hand, offers a unique opportunity to characterize the cosmic peculiar velocity field in the

⋆ E-mail: mingli@mpa-garching.mpg.de, mingli@pmo.ac.cn

© 2014 RAS

distant Universe, and to search for the so-called 'missing baryons', the bulk of the cosmic baryon density which apparently lies outside galaxies and galaxy clusters, and has yet to be identified directly at $z < 2$. Thus, SZ measurements can shed light on a number of important aspects of the non-linear galaxy formation and feedback processes which structure the low-redshift Universe, as well giving access to the cosmic flow field which is influenced by the nature of Dark Energy and by possible modifications of the theory of gravity (e.g. Keisler & Schmidt 2013).

SZ measurements are challenging since the signals are small and are buried beneath primary CMB fluctuations, instrument noise, and foreground contaminants (e.g. galactic dust and synchrotron emission, free–free emission, etc.). The measurement of kSZ effects is particularly tough, since for galaxy clusters, which provide the strongest individual signals, the kSZ amplitude is an order of magnitude smaller than the tSZ, and two orders of magnitude smaller than primary CMB fluctuations. In addition to this, unlike the tSZ which has a distinctive spectral signature, the frequency dependence of the kSZ signal is identical to that of the primary CMB fluctuations. Furthermore, for an ensemble of clusters, the signal is predicted to be symmetrically distributed about zero, making it impossible to enhance the signal to noise by stacking, as is often done for the tSZ.

Despite these difficulties, the latest generation of CMB telescopes – the South Pole Telescope (Carlstrom et al. 2011; Schaffer et al. 2011), the Atacama Cosmology Telescope (Fowler et al. 2007; Swetz et al. 2011), and the *Planck* satellite – have achieved high-resolution measurements of the CMB at millimetre wavelengths over large areas, which is enabling detailed studies of the SZ effect. In particular, the tSZ has been detected at high significance and is currently posing interesting challenges to our current understanding of structure formation and cosmological parameters (Planck Collaboration et al. 2013c,b).

There have also been several claims of detection of the kSZ. Samples of (X-ray) detected clusters combined with *WMAP* CMB maps have been used to estimate cosmic bulk flows in Kashlinsky et al. (2010); Kashlinsky, Atrio-Barandela, & Ebeling (2011); Osborne et al. (2011); Mak, Pierpaoli, & Osborne (2011); Mody & Hajian (2012). These results appear to be in tension with Λ cold dark matter (ΛCDM), but the discrepancy may not be as severe as claimed (Li et al. 2012), since it has not been confirmed by new *Planck* results (Planck Collaboration et al. 2014). More recently, a 3.8σ kSZ detection has been reported from correlations of CMB residuals about pairs of luminous red galaxies (Hand et al. 2012). This finding is in qualitative agreement with the ΛCDM expectations as inferred from cosmological hydrodnamics simulations (Dolag & Sunyaev 2013). Another approach is to use linear perturbation theory to estimate the cosmic flow field from a three-dimensional distribution of galaxies, and in this way obtain a template for the expected kSZ signal on the sky (Ho, Dedeo, & Spergel 2009; Shao et al. 2011). There has been a marginal detection of the kSZ from applying this method to the 2MASS survey (Lavaux, Afshordi, & Hudson 2013). All these examples illustrate the potential of the field and show that the quality of the data is reaching a level where cosmological and astrophysical exploitation of the kSZ effect is imminent.

In this paper, we develop and test a new but related statistical method to measure the kSZ signal. The idea is to combine a sample of independently detected galaxy clusters with a velocity field estimated by applying perturbation theory to the galaxy distribution. These two ingredients allow construction of a matched filter that optimally weights the signal from each cluster based on the noise in the CMB and velocity maps and the signal amplitude predicted from cluster scaling relations and the velocity reconstruction itself. We investigate the various sources of uncertainty in this measurement and show that our approach should yield a kSZ detection with high statistical significance (7.7σ), even with current data sets. An advantage of this scheme with respect to previous ones is that it allows kSZ measurements to be grouped into different mass bins to study the gas properties of galaxy clusters. Alternatively, they can be combined into a single measurement to constrain the relation between density and velocity fields, giving information about the law of gravity and about cosmological parameters.

Our paper is organized as follows. We first present our statistical methods, including the derivation of the matched filter for kSZ measurements (§2). In §3, we describe the way in which we create mock CMB skies including the kSZ effects expected for a realistic sample of clusters. We provide details of the application of our approach to mock data in §4. In §5, we present our results, and explore and quantify different sources of systematic errors. In the final section, §6, we discuss our results and conclude.

2 OPTIMAL MEASUREMENT OF THE KSZ EFFECT

In this section, we will present and discuss our method to measure the kSZ effect for a given set of galaxy clusters.

2.1 Matched Filter

As mentioned before, the typical amplitude of the kSZ effect is smaller than the tSZ and than the primordial CMB temperature fluctuations. Thus, it is necessary to develop the best possible estimator of the signal given all the sources of noise. Here, we choose to follow the so-called matched filter formalism.

A matched filter is a linear processing of the data, specifically designed to maximize the signal-to-noise ratio (SNR) for a set of known template signal and (additive and stochastic) noise power spectra. For the case we consider here, this means to optimally extract the kSZ signal from clusters assuming the expected signal profile, the power spectrum of CMB fluctuations, and the uncertainties in the estimates for the velocity and mass of clusters.

The first step in the formalism is to define a signal template. This is simply the expected kSZ signal, whose amplitude and spatial distribution for a galaxy cluster are given by

$$\left(\frac{\Delta T}{T_{\rm CMB}}\right)_{\rm kSZ}(\boldsymbol{\theta}) \equiv k(\boldsymbol{\theta}) = -\frac{\sigma_{\rm T}}{c}\int a\,{\rm d}\chi\, n_{\rm e}(\boldsymbol{\theta},\chi)\, v_{\rm r}(\boldsymbol{\theta},\chi)\,. \quad (1)$$

Here, $\sigma_{\rm T}$ is the Thomson cross-section and c is the speed of light, a is the expansion factor, χ is a line-of-sight distance in comoving coordinate, $v_{\rm r}$ represents the velocity of the gas along the line of sight, and $n_{\rm e}$ is the number of free electrons both as a function of θ, the angular position on the sky. The minus sign follows the convention that CMB photons gain energy when the free electrons move towards us, and thus the temperature of CMB photons increases.

Assuming that (i) the spatial distribution on the sky of free electrons inside a cluster can be described as a projected NFW profile, (ii) that the velocity field has a large correlation length (much larger than the extent of a cluster), and (iii) that the gas is fully ionized, we obtain:

$$k(\theta) = -\frac{\sigma_{\rm T} v_c}{c}\, f_{\rm b}\, \mu\, \Sigma_{\rm NFW}(\theta), \tag{2}$$

where v_c is the line-of-sight velocity of the cluster, $f_{\rm b}$ is the (cosmic) baryon fraction, μ is the number of electrons per unit of gas mass. For building the filter, we choose the spatial template profile to be

$$\tau(x) = \frac{A}{(cx)^2-1} \begin{cases} 1 - \frac{2}{\sqrt{1-(cx)^2}} \tanh^{-1}\sqrt{\frac{1-cx}{cx+1}} & 0 < x < 1 \\ 0 & x = 1 \\ 1 - \frac{2}{\sqrt{(cx)^2-1}} \tan^{-1}\sqrt{\frac{cx-1}{cx+1}} & x > 1, \end{cases} \tag{3}$$

c is the cluster's concentration parameter, $x = r/r_{200} = \theta/\theta_{200}$ the dimensionless radius. A is a constant normalizing the template profile at $x = 0$, so when this filter is located on the centre of a cluster, it will return a statistically unbiased amplitude of the kSZ signal. We note that our approach and results do not depend on assuming this particular functional form, the only requirement is to the correct profile to be know. Our choice (a projected NFW profile) is justified here since in our forthcoming tests we assume that the spatial distribution of baryons follows that of the DM. However, when applied to real data, a different, observationally motivated profile might be preferred.

The next step is to define $P(\boldsymbol{k})$, the power spectrum of the noise. In Fig. 1, we show the contribution to the total angular CMB power spectrum of different components for a *Planck*-like experiment: primordial anisotropies (blue line), instrumental noise (orange line) and kSZ (green line). Here we can see that the kSZ signal is sub-dominant at all scales. In consequence, we approximate the noise in our kSZ estimates as the power spectrum of primordial CMB fluctuations plus the noise contribution, that is $P = P_{\rm CMB}|\hat{B}|^2 + P_{\rm noise}$.

The shape of the matched filter is set by requiring a minimum variance estimator. Following Haehnelt & Tegmark (1996); Melin, Bartlett, & Delabrouille (2005, 2006), in our case it is possible to show that the Fourier transform of the filter is given by

$$\hat{\Psi}(\boldsymbol{k}) = \sigma^2 \frac{\hat{\tau}(\boldsymbol{k})\hat{B}(\boldsymbol{k})}{P(\boldsymbol{k})}, \tag{4}$$

where $\hat{\tau}$ is the Fourier transform of the signal profile, $\hat{B}(\boldsymbol{k})$ is the beam function of a given CMB experiment which we assume follows a Gaussian profile. The variance of the filtered input data is denoted by σ^2:

$$\sigma^2 = \left[\int \frac{|\hat{\tau}(\boldsymbol{k})\hat{B}(\boldsymbol{k})|^2}{P(\boldsymbol{k})} \frac{{\rm d}^2k}{(2\pi)^2}\right]^{-1}. \tag{5}$$

In Fig. 2, we show the resulting filter $\Psi(\theta)$, for a cluster (with mass around $10^{14}h^{-1}{\rm M}_\odot$ and $z \sim 0.1$) with an angular size of 10 arcmin on the sky. By comparing the solid black and dot−dashed blue lines, we can see how the filter is modified when the instrument noise in considered in addition to the primary anisotropies in the CMB. For comparison, we show the assumed beam profile as a dashed red line. We note that we have checked the impact of uncertainties in the determination of the centre of clusters (c.f. §5.2.2). In this case, the amplitude of the filter changes, but its shape remains largely unaffected due to the dominating effect of the beam size of the *Planck* experiment. This, however, might be different for higher resolution CMB experiments.

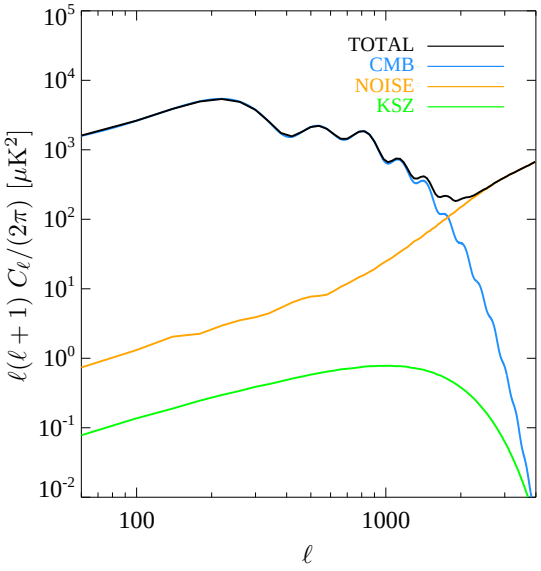

Figure 1. Angular power spectra of one realization of our simulated *Planck* SMICA-like sky maps. Three components are shown as CMB (blue solid line), instrument noise (orange solid line) and KSZ (green solid line). All power spectra have been convolved with a beam function with FWHM=5 acrmin.

In general, the central value returned by the filter refers to the signal integrated over a patch on the sky of a given radius (a cone in three dimensions). Here, we choose to integrate up to three times the size of the target cluster, though our results are not sensitive to the exact integration limit. Due to the large coherence length of the cosmic velocity field, integrating outside the clusters boundary has the advantage of including material that is likely to be moving with the target cluster (c.f. §3.2). Thus, our kSZ measurement corresponds to $K^{\rm cyl}_{3r_{200}}$, the total signal within a cylinder of aperture radius $3 \times r_{200}$ (where r_{200} is the radius containing a mean density equal to 200 times the critical value in the Universe). This measurement can be scaled to the expected signal produced by a spherical halo, K_{200}, by the following quantity:

$$\frac{K^{\rm cyl}_{3r_{200}}}{K_{200}} = \frac{\int_0^\infty {\rm d}r \int_{r\sin\theta<3r_{200}} {\rm d}\theta\, \rho(r) 2\pi r^2}{\int_0^{r_{200}} {\rm d}r \rho(r) 4\pi r^2}, \tag{6}$$

where $\rho(r)$ is given by $\rho(x) = \frac{\rho_0}{x(1+x)^2}$, ρ_0 is a characteristic density, and $x = r/r_{200}$. Supposing cluster mass M_{200} (cluster mass within r_{200}) can be inferred from other observed properties, we can obtain an estimation of cluster's velocity through relation

$$K_{200} = -\frac{\sigma_{\rm T} v_c}{c}\, f_{\rm b}\, \mu\, M_{200}. \tag{7}$$

At this point, this estimator also contains contributions from the tSZ effect, point sources, etc. As we will see next, if there is an external estimate for the velocity field, then these extra terms will vanish and we can recover a clean measurement of the kSZ effect which can be used to constrain the law of gravity, cosmological parameters and gas properties in our cluster catalogue.

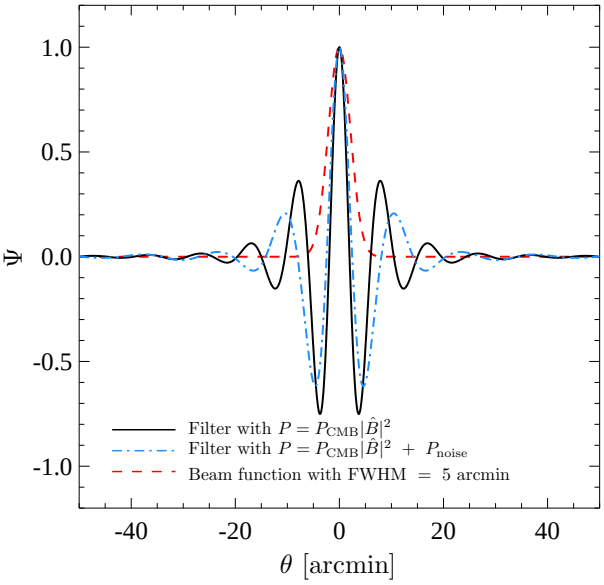

Figure 2. An example of matched filter for a cluster with a angular scale $\theta_{200} = 10$ arcmin. The black solid line shows the radial filter profile when noise power spectrum $P(\boldsymbol{k})$ in equation (4) only contains CMB component. The filter when both CMB and instrument noise are contained in $P(\boldsymbol{k})$ is shown as blue dotted−dashed line. The red dashed line gives a reference of a beam function with FWHM=5 acrmin.

2.2 The velocity field

In linear theory, and assuming a linear bias, the peculiar velocity field is directly proportional to the logarithmic derivative of the growth rate and to the galaxy overdensity field. Explicitly, the Fourier transform of the velocity field is

$$\boldsymbol{v}(\boldsymbol{k}) = -\boldsymbol{i}\beta(z)H_0\delta_{\rm g}(\boldsymbol{k})\frac{\boldsymbol{k}}{k^2}\,, \tag{8}$$

with $\beta(z) = f(\Omega_{\rm m}, z)/b_{\rm g}(z)$, $b_{\rm g}$ is the galaxy bias, H_0 is the Hubble constant and $f(\Omega_{\rm m}, z) \equiv \frac{{\rm d}\ln D(z)}{{\rm d}\ln a}$, where $D(z)$ is the growth factor and a is the expansion factor.

Thus, on large scales (where these relations hold) the observed galaxy distribution can be used to obtain an estimate of the velocity of galaxy clusters. Note also that there are equivalent expressions in higher order perturbation theory. These can achieve higher accuracies and are valid down to smaller scales (Kitaura et al. 2012b).

Contrasting the reconstructed velocities with the measurements obtained by our matched filter for a cluster i, one can constrain a parameter α:

$$\alpha_i = -\frac{c}{\sigma_T\, f_{\rm b}\,\mu}\frac{K_{200,i}}{M_{200}}\frac{1}{v_{{\rm rec},i}}, \tag{9}$$

$$= \frac{v_{\rm kSZ,i}}{v_{\rm rec,i}} + \frac{\epsilon_i}{v_{\rm rec,i}}, \tag{10}$$

where ϵ captures all other sources to CMB temperature fluctuations inside clusters (e.g. tSZ, point sources, etc.). The measurement from individual clusters can be combined into a single measurement of the α parameter

$$\alpha = \frac{\sum_i \alpha_i\, w_i}{\sum_i w_i}, \tag{11}$$

with the associated error

$$\sigma_\alpha = \left[\frac{1}{\sum_i w_i}\right]^{1/2}. \tag{12}$$

Since ϵ is expected to be uncorrelated with the velocity field, and the sign of $v_{\rm rec}$ changes from one cluster to another, so the expectation value of $\epsilon/v_{\rm rec}$ is zero. Therefore if α is equal to the unity, this means that the gravity model and cosmological parameters assumed are supported by the kSZ data. Otherwise, $\alpha \neq 1$, a different model is preferred. In other words, this ratio constrains directly $\beta/\beta_{\rm fid}$, where $\beta_{\rm fid}$ is the fiducial value of β assumed in computing the velocities from the galaxy distribution.

It is important to emphasize that this method is based on the assumption that reconstructed velocity has the correct sign, so that after effectively weighting individual kSZ measurements by the SNR expected for each cluster, all available signals are optimally combined together. For instance, regions with a velocity close to zero, are expected to contribute mostly to the noise, not the signal, and are therefore given less importance in the final measurement.

Additionally, the weight factors can be modified to include all uncertainties affecting the measurement. In our case, there are two major sources: one is intrinsic to the kSZ measurement (we label it with $\sigma_{\rm kSZ}$), the second is in the uncertainty in the velocity estimation due to a given reconstruction method (labelled as $\sigma_{\rm rec}$). If the two contributions are uncorrelated, the weight assigned to each cluster is

$$w_i^{-1} = \left(\frac{1}{v_{\rm rec,i}}\right)^2\left(\sigma^2_{\rm kSZ,i} + \sigma^2_\epsilon + \beta^2_{\rm fid}\sigma^2_{\rm rec,i}\right). \tag{13}$$

Both of $\sigma_{\rm kSZ}$ and $\sigma_{\rm rec}$ vary from cluster to cluster, and σ^2_ϵ is approximately proportional to the inverse of the number of systems averaged over. If we assume that the uncertainty arises mainly due to the kSZ measurement, then equation (13) is simplified to

$$w_i^{-1} = \left(\frac{1}{v_{\rm rec,i}}\right)^2\sigma^2_{\rm kSZ,i}. \tag{14}$$

For the remainder of this paper, we will present our results based on this simplified form of the weight factor. We further discuss uncertainty related to velocity reconstruction in §5.3.1.

3 MOCK OBSERVATIONS

In this section, we describe the mock kSZ observation we have created to test and assess the performance of our approach.

3.1 The MXXL simulation

We build kSZ mocks based on the Millennium-XXL (MXXL) simulation (Angulo et al. 2012). The MXXL simulation uses 6720^3 particles to follow the distribution and evolution of DM within a cubic volume with a comoving side length of $3\,h^{-1}{\rm Gpc}$. The mass of each simulation particle is $m_{\rm p} = 6.17\times10^9 h^{-1}{\rm M}_\odot$, thus we

resolve galaxy clusters with tens of thousands of particles. The cosmological parameters match those of the previous two Millennium simulations (Springel et al. 2005; Boylan-Kolchin et al. 2009).

The MXXL simulation combines a large volume and a relatively high-mass resolution. Simultaneously fulfilling these conditions posed a serious challenge to supercomputational facilities in terms of raw execution time, RAM requirements, I/O load and long-term storage. In order to alleviate these, the full particle data were stored at redshifts $z = 0$, 0.25, 1 and 3. Self-bound halo and subhalo catalogues, among other data products were produced on-the-fly. For further information, we refer the reader to Angulo et al. (2012).

Most important for our purposes is the fact that this simulation produces a suitable DM backbone for our kSZ modelling. This provides a realistic catalogue of DM clusters as well as a fully non-linear velocity field with all the features and correlations we expect in ΛCDM, including the non-negligible contribution of large Fourier modes.

3.2 Light-cone and the kSZ effect

We build a light-cone using the $z = 0.25$ snapshot from the MXXL, and considering all particles within a sphere of $1500\,h^{-1}\mathrm{Mpc}$ radius. This produces an all-sky light-cone up to $z = 0.56$, without any repetition of the simulation box. Note that this procedure effectively neglects the evolution of the mass clustering along the line of sight; however, this is a reasonable approximation given the restricted redshift range we consider. We also build a light-cone with the position and velocities of all haloes in our catalogue.

Then, we assume that all the gas in the Universe is ionized and that the position and velocity of baryons follow those of DM. This is a reasonable approximation on large and intermediate scales (Angulo et al. 2013). Thus, the kSZ effect integrated over a area element in our simulated sky is given by the discrete version of equation (1)

$$\left(\frac{\Delta T}{T}\right)_{\rm kSZ} = k = -\frac{\sigma_{\rm T}\, f_{\rm b}\, \mu}{c} \sum_i \frac{v_{{\rm r},i}\, m_{{\rm dm},i}}{{\rm d}\Omega_{\rm pix} D_{{\rm a},i}^2}\ , \qquad (15)$$

where the summation runs over all particles that contribute to the given area element on the sky, $D_{\rm a}$ is the angular diameter distance and ${\rm d}\Omega_{\rm pix}$ is the solid angle of the area element.

We pixelize our sky map using the `HEALPix` software (Górski et al. 2005)[1] with $N_{\rm side} = 2048$ pixels. This corresponds in total to 50 331 648 elements, each of which covers an area equal to $1.43^{-5}\ \mathrm{deg}^2$.

In Fig. 3 we show a Mollweide representation of our kSZ sky. The mean of the map corresponds to a value of $\langle \Delta T_{\rm kSZ} \rangle = 0.12\ \mu$K with variance $\sigma = 1.36\ \mu$K. The actual power spectrum of the simulated kSZ is shown by the green line in Fig. 1. Note that the map shows a large coherence length, with regions of similar amplitude extending over large fractions of the sky. This is a consequence of the large correlation length of the velocity field expected in CDM density power spectra, where velocity fluctuations receive significant contributions from very large modes. The inset in this figure shows a zoom to the fluctuations inside a $16\,\mathrm{deg}.6$ patch (approximately $200\,\mathrm{Mpc}$ wide at $z = 0.25$).

Finally, we mimic *Planck* CMB observations. The *Planck* satellite observes the sky in nine frequency channels from 30 to 875 GHz, the angular resolution ranges from 33 arcmin for the lowest frequency channel down to 5 arcmin for the highest. In this work, we only focus on the SMICA-like CMB map, which is a foreground-cleaned map. In consequence, we directly simulate the sky map that only contains CMB and kSZ components. After generating the map, we smooth the map with a Gaussian kernel with FWHM=5 arcmin (angular resolution of *Planck* SMICA map). Posteriorly, we will also include the corresponding instrument noise.

[1] `http://healpix.jpl.nasa.gov/`

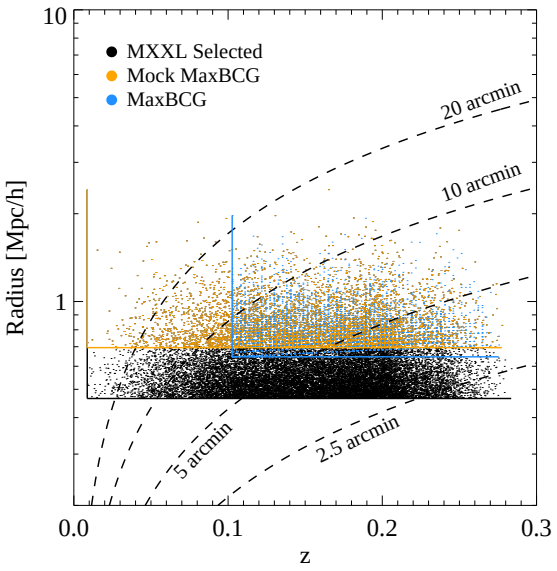

Figure 4. The distribution of clusters used in this work on the radii and redshift plane. The black dots and yellow dots are clusters in each catalogue. The MaxBCG clusters are also shown (blue dots), assuming the same cosmology as MXXL simulation. The solid lines around clusters indicate selection boundaries we use to construct the catalogues. The black dashed lines are here to lay out the relation of cluster radius for fixed angular size as a function of redshift.

3.3 Cluster Catalogue

For our analysis, we consider two different cluster catalogues. We restrict the samples to a volume similar to that of the SDSS, over which there are reconstructed density and velocity fields (Kitaura et al. 2009; Jasche et al. 2010b).

1) MXXL selected: our first sample contains all haloes in our light-cone with mass above $1.5 \times 10^{13} h^{-1}\mathrm{M}_\odot$. This contains 24529 objects.

2) Mock MaxBCG: our second sample employs a higher mass cut, $5 \times 10^{13} h^{-1}\mathrm{M}_\odot$, which roughly corresponds to a threshold in optical richness of 10 for the MaxBCG catalogue (Koester et al. 2007). This extra condition reduces the number of clusters in this catalogues down to 5663.

We summarize the main properties of our samples in Table 1. In Fig. 4, we show the redshift and size of the clusters in our samples. These properties will help us to understand the contribution of different types of clusters to the total SNR for the kSZ measurements. We can see that given our selection criteria most systems are found at redshifts below 0.3. This validates the redshift range

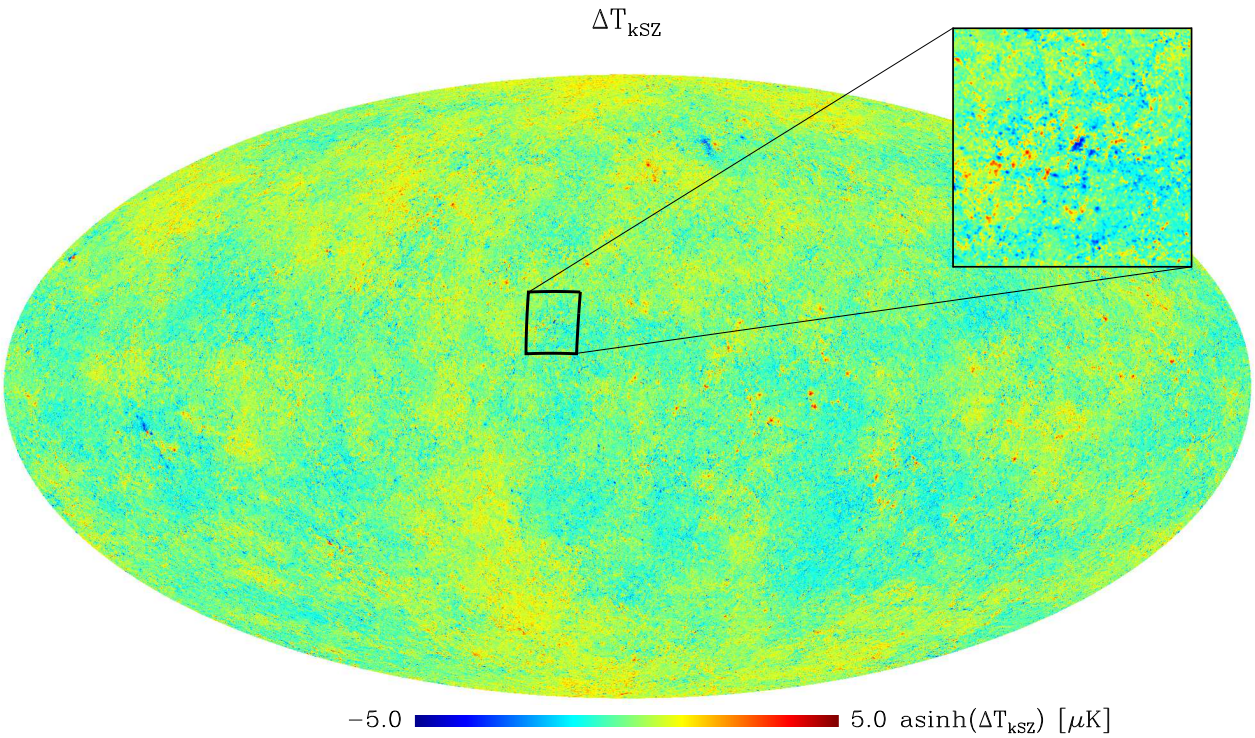

Figure 3. Simulated all-sky map of the kSZ signal with a resolution of $N_{\rm side} = 2048$. The map is smoothed with a beam function with FWHM=5 acrmin and is colour-coded by arcsinh($\Delta T_{\rm kSZ}$). The overlaid panel shows a patch with side length of $14^\circ.66$, zooming in around a prominent structure which produces a clear kSZ signal.

covered by our kSZ light-cone. For comparison, we also show the properties of MaxBCG cluster catalogue. We note that the mass cut-off of our Mock MaxBCG catalogue roughly coincides with the observational catalogue. Because no selection function is applied, our Mock- MaxBCG sample contains 28 per cent more clusters than the real one, most of these additional clusters have redshifts below ~ 0.1.

Another issue should be noted is that our catalogues are built from a single snapshot at $z = 0.25$, the mass cut shows a constant radius threshold across whole redshift range in Fig. 4. But cluster with the same mass does not have a constant physical radius at different redshift, because the M_{200} and R_{200} are linked by $\rho_{\rm crit}(z)$. So for real cluster catalogue, the mass cut-off should not correspond to a constant radius threshold. But this is a minor issue, and will not affect our analysis and results.

Table 1. Halo catalogue used in this work

Cata. name	M_{200} range ($\times 10^{10} h^{-1}{\rm M}_\odot$)	θ_{200} range (degree)	Number
MXXL selected	(1500, 210885)	(0.035, 1.897)	24529
Mock MaxBCG	(5000, 210885)	(0.052, 1.897)	5263
MaxBCG	(5082, 144073)	(0.052, 0.374)	4058

Note: For clusters in real MaxBCG catalogue, the cluster mass is computed with $M_{200} - N_{200}$ provided by Hilbert & White (2010). The cluster angular size is computed under the same cosmology model as MXXL simulation.

3.4 Reconstructed velocity field

As discussed before, the peculiar velocity of galaxy clusters can be estimated using perturbation theory and a three-dimensional distribution of galaxies. Naturally, there are uncertainties associated with this procedure, thus, in order to explore the impact of these, for our analysis, we consider three different types of velocity fields.

1) $v_{\rm halo}$: These correspond to the true velocity of the cluster, as computed by the centre of mass velocity of the parent FOF halo. Naturally, this corresponds to the best possible estimation, and it is useful to differentiate the impact of the uncertainties in the velocities from other sources.

2) $v_{\rm rec}$: These correspond to velocities estimated from the DM density field with linear perturbation theory. In practice, we compute these by the mapping DM particles on to a grid using a Clouds-in-Cell (CIC) assignment scheme, with a spatial resolution of $1.5\,h^{-1}{\rm Mpc}$. Then, we smooth the density field with a Gaussian kernel of size $r_{\rm s} = [2.5, 5, 10]\,h^{-1}{\rm Mpc}$, and use the smoothed field as a source in equation (8) to obtain an estimate for the velocity field. Finally, we interpolate this field to the positions of clusters.

3) $v_{\rm CIC}$: We generate another velocity field by directly mapping the velocity of DM particles on to a grid using the CIC assignment scheme. We then smooth this field using Gaussian kernels of size $r_{\rm s} = [2.5, 5, 10]\,h^{-1}{\rm Mpc}$, and interpolate back to the clusters positions.

4 KSZ AND α MEASUREMENTS

Now we are in position to apply our matched filter procedure to the simulated kSZ+CMB sky, and using the different cluster catalogues and velocity estimates discussed in the previous section.

At the position of each cluster, we convolve the CMB maps with the matched filter. We do this in Fourier space and on a patch of side length of $14^\circ.66$ and 512×512 pixels, which makes patches have the same angular resolution as the original sky map. The patch size is chosen to be large enough to ensure a representative assessment of background noise. The characteristic size of the filter is set by the cluster's apparent size on the sky and by using the concentration−mass relation of proposed by Duffy et al. (2008).

The value of α is estimated for each cluster in our catalogues (equation (9)) and the combined measurement is given by taking the ensemble weighted mean (equation (11)).

In order to assess the advantages of the matched filter approach, we perform another measurement of the kSZ signal using a simple aperture photometry method (AP filter). The kSZ flux is estimated as the total kSZ flux within a circular area of radius R_1 minus the expected background, which is set by the average kSZ flux in a annulus of dimensions $R_1 = 3 \times r_{200}$ and $R_2 = \sqrt{2}\,R_1$. Therefore, the kSZ signal within a cylinder of aperture radius $3 \times r_{200}$, (analogous to the quantity measured by the matched filter) is given by

$$K^{\rm cyl}_{3r_{200}} = K_{[0,R_1]} - K_{[R_1,R_2]}. \qquad (16)$$

Following Planck Collaboration et al. (2014), the uncertainty for the measurement about each cluster is set as the rms fluctuation of the AP filter applied at 100 randomly chosen positions. As in the case of matched filters, the value of α_i for each cluster is the weighted by its uncertainty and in this way a global α is computed.

5 RESULTS

In this section, we test the ideas presented before, and assess their performance when applied to mock kSZ observations. We will start with the simplest case, in which a perfect cluster catalogue and velocity fields are assumed to be known. Then, we progressively increase the realism of the cases we consider and include further sources of uncertainty. In all cases, we explore different estimates of the velocity field and the two cluster catalogues described in §3.3, unless otherwise stated. The main results are summarized in Tables 2 and 3 and Fig. 7.

We note that if our measurement of α is equal to the unity, our method would provide an unbiased estimate of the relation between density and velocity, which is captured by the β parameter. The uncertainty in α can be regarded as the accuracy with which β is measured.

5.1 CMB primary anisotropies, residuals and instrument noise

We start by considering the CMB primary anisotropies as the only source of uncertainty in α. We applied the procedure outlined in the previous section to 50 realizations of the CMB sky. The results are provided in the 4th column in Table 2 (labelled as 'CMB'). The mean measured value of α is 0.963 ± 0.0046 for the Mock-MaxBCG sample. For the more abundant MXXL sample is 0.977 ± 0.0035, which shows a similar bias in α but the statistical error decreases. This is the first validation of the performance of our matched filter approach.

Even though the component separation procedure could provide a foreground cleaned CMB map, some residuals are still left over as contaminations. Since our measurements are performed at individual clusters, tSZ residuals are more likely to add-up coherent contaminations to our results, showing up as the term ϵ in equation (9). We initially presume that $\epsilon/v_{\rm rec}$ goes to zero when averaging over whole cluster samples. In order to check further how true this assumption is, we generate a tSZ map with the same data set, and then a few per cent amplitude of the tSZ signal is added to the CMB + kSZ map as residual. We test 1, 5 and 10 per cent tSZ amplitudes and find that residual in term $\epsilon/v_{\rm rec}$ almost gone and bias up the final α with less than 1, 4 and 7 per cent, respectively. So we think at a few per cent level, residual would have little impact on α estimation.

Another important source of uncertainty on small scales is the instrument noise. As shown in fig. E.3 of Planck Collaboration et al. (2013a) and in Fig. 1, at the scale of our Mock-MaxBCG clusters (around 6 arcmin or $\ell \sim 1600$), the typical amplitude of this noise is similar to that caused by primary CMB anisotropies. In our formulation of the matched filter this contribution is implicitly taken into account, since we use the power spectrum of our sky map itself as the noise term in equation (4).

In order to assess the impact on this extra noise contribution on α, we have generated 50 independent maps of the CMB primary fluctuations plus *Planck* product SMICA-like instrument noise. We apply our matched filter approach and show the result in the 5th column in Table 2 (labelled as 'CMB+Noise'). As expected, the mean value of α remains the same, since this new noise component is uncorrelated with the signal. The associated uncertainties, however, roughly double.

We note that the uncertainties on α estimated from the variance across 50 sky realizations and by the matched filter procedure agree remarkably well. For instance, when only CMB sky included, the scatter on α from the 50 sky realizations is 0.0459, compared with matched filter output value of 0.0455. For the case of 'CMB+Noise', the value is 0.089 compared with 0.096. A further support for our implementation of the matched filter approach can be obtained by comparing the results provided above with those obtained from a simple AP filter, which are provided in the 2nd and 3rd columns of Table 2. Even though the estimated α for all cases is consistent with those obtained using a matched filter, the statistics errors quoted are a factors of $20-30$ larger and are comparable with the level of the signal itself. These two facts support the statistical validity and advantage of our formulation.

In all the cases, we have considered so far there is a small bias in α, $\alpha \neq 1$ roughly at the 1σ level. We have checked that this originates from the fact that the peculiar velocity measured from the kSZ is actually a mass-weighted average over a cylinder on the sky of size $3\times r_{200}$. This is not necessarily identical to the centre of mass velocity of the cluster. This explains why the bias is slightly larger in the MXXL cluster which contains less massive clusters. Nevertheless, we will see that the systematic biased introduced are smaller than the statistical uncertainty introduced by other sources of noise, and thus validates our modelling given the accuracy with which current measurements are possible.

Table 2. Estimated mean α value comparison with 50 realizations of sky, between cluster catalogues, Ap filter and matched filter, with/without instrument noise

	Mock MaxBCG				MXXL selected	
v used in reference	CMB AP filter	CMB + Noise AP filter	CMB	CMB + Noise	CMB	CMB + Noise
$v_{\rm halo}$	1.028 ± 1.103	1.026 ± 1.106	0.963 ± 0.046	1.011 ± 0.096	0.977 ± 0.035	1.029 ± 0.075
$v_{\rm rec,r_s=2.5\,h^{-1}Mpc}$	0.792 ± 0.933	0.788 ± 0.935	0.794 ± 0.038	0.837 ± 0.080	0.831 ± 0.030	0.875 ± 0.065
$v_{\rm rec,r_s=5\,h^{-1}Mpc}$	0.967 ± 1.131	0.964 ± 1.134	0.969 ± 0.046	1.018 ± 0.097	0.988 ± 0.036	1.040 ± 0.078
$v_{\rm rec,r_s=10\,h^{-1}Mpc}$	1.040 ± 1.352	1.041 ± 1.356	1.072 ± 0.055	1.125 ± 0.115	1.082 ± 0.043	1.138 ± 0.092
$v_{\rm CIC,r_s=2.5\,h^{-1}Mpc}$	1.039 ± 1.163	1.036 ± 1.166	1.021 ± 0.048	1.071 ± 0.100	1.029 ± 0.037	1.084 ± 0.080
$v_{\rm CIC,r_s=5\,h^{-1}Mpc}$	1.055 ± 1.261	1.054 ± 1.264	1.051 ± 0.051	1.101 ± 0.108	1.058 ± 0.040	1.114 ± 0.086
$v_{\rm CIC,r_s=10\,h^{-1}Mpc}$	1.083 ± 1.428	1.086 ± 1.432	1.105 ± 0.058	1.161 ± 0.121	1.108 ± 0.045	1.168 ± 0.097

Table 3. Estimated mean α value with 50 realizations of considered mass scatter and miscentring effects.

	Mock MaxBCG					
v used in reference	CMB + Noise	CMB + Noise + velocity systematics	CMB + Noise + Mass scatter	CMB + Noise + miscentring without correction	CMB + Noise + miscentring with correction	CMB + Noise + miscentring with correction + Mass scatter
$v_{\rm halo}$	0.959 ± 0.096	0.957 ± 0.097	0.970 ± 0.099	0.730 ± 0.097	0.955 ± 0.126	1.026 ± 0.130
$v_{\rm rec,r_s=2.5\,h^{-1}Mpc}$	0.757 ± 0.080	0.757 ± 0.081	0.776 ± 0.083	0.588 ± 0.082	0.751 ± 0.105	0.793 ± 0.107
$v_{\rm rec,r_s=5\,h^{-1}Mpc}$	0.951 ± 0.097	0.949 ± 0.099	0.971 ± 0.101	0.734 ± 0.099	0.952 ± 0.128	1.014 ± 0.132
$v_{\rm rec,r_s=10\,h^{-1}Mpc}$	1.111 ± 0.115	1.112 ± 0.117	1.137 ± 0.119	0.862 ± 0.117	1.127 ± 0.152	1.202 ± 0.156
$v_{\rm CIC,r_s=2.5\,h^{-1}Mpc}$	1.014 ± 0.100	1.011 ± 0.102	1.029 ± 0.104	0.776 ± 0.102	1.011 ± 0.132	1.080 ± 0.136
$v_{\rm CIC,r_s=5\,h^{-1}Mpc}$	1.067 ± 0.108	1.066 ± 0.110	1.086 ± 0.112	0.821 ± 0.110	1.069 ± 0.142	1.142 ± 0.147
$v_{\rm CIC,r_s=10\,h^{-1}Mpc}$	1.181 ± 0.121	1.183 ± 0.123	1.206 ± 0.126	0.915 ± 0.123	1.197 ± 0.160	1.279 ± 0.165

Note: The results are estimated with one particular realization of CMB+Noise sky and 50 realizations of mass scatter and miscentring effects. The measurements without these two effects are listed in 2nd column, and results with velocity uncertainties are listed in 3rd column.

5.2 The uncertainties in the cluster catalogue

We now consider the impact of uncertainties in estimating cluster masses observationally. Also we address the difficulty of optical cluster finders algorithms to identify the clusters centre of mass.

5.2.1 The mass–richness relation

The mass of a cluster is not a direct observable, one has to infer it from other observed properties (e.g. optical richness, strong and weak gravitational lensing signal, X-ray luminosity or tSZ flux signal). Although the mean relations can be calibrated observationally or using numerical simulations, deviations of individual clusters from the mean relation lead to a scatter on the estimated cluster mass. Furthermore, there are other sources of scatter in the observable–mass relationship related to line-of-sight contamination, the dynamical state and triaxiality of the parent halo, etc. This affects the shape of matched filter and its normalization, and therefore this introduces a further source of uncertainty in the estimated velocity of a cluster from its kSZ signal.

Here, we explore this effect in the case of a optically-detected cluster catalogue, such as the MaxBCG sample. The mass–richness relation and its scatter for such catalogue have been studied with both observations (Johnston et al. 2007) and simulations (Hilbert & White 2010; Angulo et al. 2012). For example, Angulo et al. (2012) give a mean relation which is described by a power law $\langle M_{200}\rangle = M^{1.07}$, with a lognormal scatter $\sigma_{\log_{10}(M_{200})} = 0.36$. In order to incorporate this effect in our simulations, we assign a richness to each cluster according the following procedure.

We utilize the results provided by Hilbert & White (2010), that the mean mass $\langle M_{200}\rangle$, the lognormal scatter of mass $\sigma_{\log_{10}(M_{200})}$ and cluster number density n are given for various richness N_{200} bins. With these pieces of information cluster mass distribution at each richness bin $\mathrm{pdf}(M_{200})$ can be constructed, therefore the cluster mass function is just summation over contributions from all richness bins,

$$\mathrm{d}n(M_{200})/\mathrm{d}M_{200} = \sum_{i=1}^{N_{\rm bins}} n_i \mathrm{pdf}_i(M_{200}), \qquad (17)$$

then this function is normalized by the total number of clusters in our Mock-MaxBCG catalogue. After that, we divide clusters in our catalogue into several different logarithmic mass bins. In each of these bins, clusters are assigned a richness according to the probability $\mathrm{pdf}_i(M_{200})$.

Once each cluster has a richness value, we use the mean mass–richness relation to assign an estimate for the cluster mass. Then, we construct the corresponding filters and repeat our analysis. The results are shown in the 4th column of Table 3. We find that the average α and its uncertainty both vary by less than 5 per cent. This is in agreement with previous works which showed that the scatter in mass does not have a significant impact on filter-recovered tSZ signal (Biesiadzinski et al. 2012; Planck Collaboration et al. 2014). This is a consequence of the shape of the matched filter being

weakly dependent on cluster mass as a result the concentration and cluster size depend weakly on halo mass. Moreover, the uncertainty on mass estimation is subdominant compared to the other sources of uncertainties related to the CMB maps.

The above discussion is based on the hypothesis that the mean mass–richness relation could provide unbiased mass estimations for clusters in fixed richness bin. While the mass–richness relation is usually obtained by lensing mass calibrations. But lensing mass estimates are very difficult, mass–richness relations obtained by different lensing mass calibrations already show an important discrepancy (Johnston et al. 2007; Rozo et al. 2009). This would introduce a potential systematic effect on estimating cluster mass, and consequently would take effect when translating kSZ flux into velocity estimation (equation (9)). In order to examine the systematic bias of mass–richness relation on α, we shift the mean relation by 10, 20, 40 per cent high (low), then we find that α estimation will be biased 6, 10, 18 percent low (6, 14, 34 per cent high), respectively. This may act as an important systematic bias in our method. It is still not clear how well can different mass–richness relations represent cluster mass and its observable. It is hard to make a specific quotation here, so we put three bias levels for reference.

5.2.2 *The cluster miscentring*

Another effect that may seriously hamper our efforts to get an accurate value of α is the offset between the centre of mass of a cluster and the centre estimated using its optical properties. A BCG misidentification and astrophysical processes may both cause this so-called miscentring (Johnston et al. 2007; Hilbert & White 2010).

We estimate the impact of this effect by randomly selecting a fraction of clusters, $p_{\rm c}$, to be miscentred: from 40 per cent for the lowest richness bin down to 20 per cent for the highest richness bin, and then perturb their centre according to

$$\mathrm{pdf}(R_{\rm off}) = \frac{R_{\rm off}}{\sigma^2_{\rm off}} \exp\left(-\frac{R^2_{\rm off}}{2\sigma^2_{\rm off}}\right) , \qquad (18)$$

where $\sigma_{\rm off} = 0.42\,h^{-1}{\rm Mpc}$ (Hilbert & White 2010). This expression describes the distribution of projected distances between the identified centre and the centre of mass of a cluster.

We repeat our analysis for the new centres. We find a strong decrease in the estimated value of α of about 20 per cent. The reason for this is that the incorrect cluster convolved with the matched filter results in a heavy under estimation of the clusters mass and kSZ signal. One way to reduce the problem is to modify the matched filter with an effective kSZ signal profile that correctly describes the presence of a set of miscentred clusters.

The kSZ signal of clusters in a given mass can be described as a weighted average of the profile of correctly and incorrectly centred objects. Correctly centred clusters have a mean kSZ profile given by equation (3). The signal of miscentred clusters is a convolution by azimuthal angle of the offset distribution with the correctly centred profile:

$$\tau_i(R|R_{\rm off}) = \frac{1}{2\pi}\int_0^{2\pi} {\rm d}\theta\, \tau_i\left(\sqrt{R^2 + R^2_{\rm off} + 2R\,R_{\rm off}\cos(\theta)}\right) . \qquad (19)$$

Assuming that the offset distribution is given by equation (18), the mean kSZ profile of miscentred cluster can be written as a average over the distribution:

$$\tau_i^{\rm mis}(R) = \int {\rm d}R_{\rm off}\ \mathrm{pdf}(R_{\rm off})\ \tau_i(R|R_{\rm off}). \qquad (20)$$

Finally the mean kSZ profile for clusters in a given mass bin i is

$$\tau_i^{\rm tot}(R) = (1-p_{\rm c})\,\tau_i + p_{\rm c}\,\tau_i^{\rm mis}. \qquad (21)$$

The new profile has a core, which compensates the total integrated kSZ flux signal with a statistically correct answer. We have repeated our analysis with the new matched filters, and show the results in the 6th column of Table 3. Indeed, after this correction, we recover a statistically unbiased estimation of α. This is a dramatic improvement compared to the results without considering the miscentring problem. The price for this in an increment of about 25 per cent in the uncertainty with which we measure the kSZ effect. We note, however, that this effect also needs to be considered in any other interpretation of the correlation between galaxies and the kSZ signal, and in any other quantity estimated from template fitting (e.g. the SZ decrement).

5.3 Peculiar velocities

When dealing with observations, the velocity of clusters is unknown, and one needs to resort to indirect estimations. In order to assess the impact of this, we repeat our measurements, but now employing different estimations for the velocity of clusters, as listed in §3.4. The results are provided in the $2-4$th rows and in the $5-7$th rows for velocities estimated using linear theory and CIC interpolation, respectively.

In the case of CIC velocities, $v_{\rm CIC}$, we see that the $2.5\,h^{-1}{\rm Mpc}$ smoothing provides an unbiased estimate of α, whereas the 5 and $10\,h^{-1}{\rm Mpc}$ smoothing overestimate its value (i.e. underestimate the clusters velocity) by roughly 1σ and 2σ.

In the case where reconstructed velocities, $v_{\rm rec}$ are considered, we see that the smallest smoothing scale returns a value for α between 20 and 25 per cent smaller than the unity. For larger smoothing scales, the underestimation decreases and for the $10\,h^{-1}{\rm Mpc}$ smoothing, we recover a (biased) value consistent with that in the case of CIC. However, uncertainties are about 30 per cent larger in the latter case.

Now we explore these results further. In Fig. 5, we show one-to-one comparisons between clusters true line-of-sight velocity, and (i) the CIC smoothed velocities (top panels) and (ii) reconstructed velocities based on linear theory (bottom panels). As stated before, we consider three smoothing scales, $r_{\rm s}$ =2.5, 5 and $10\,h^{-1}{\rm Mpc}$.

In all cases, we see a strong correlation between the true and estimated velocities. The scatter increases as we consider larger smoothing scales, and also the scatter for reconstructed velocities is larger than for CIC velocities. Also, for both estimation methods, we see that the velocities are systematically underestimated for large smoothing scales. This can be seen more clearly by comparing the 1:1 relation (red line) with the blue diagonal line, which shows the median value of velocity estimated in bins of $v_{\rm halo}$. Note that the slope of the relation for the case of reconstructed velocities is always steeper than the CIC counterparts, which is a consequence of linear perturbation theory breaking down and overestimating the divergence of the velocity field and thus of its line-of-sight component (see also fig. 7 of Kitaura et al. 2012b).

Overall, we appreciate that the estimated velocity field is a balance between two competing effects: (i) the accuracy of linear per-

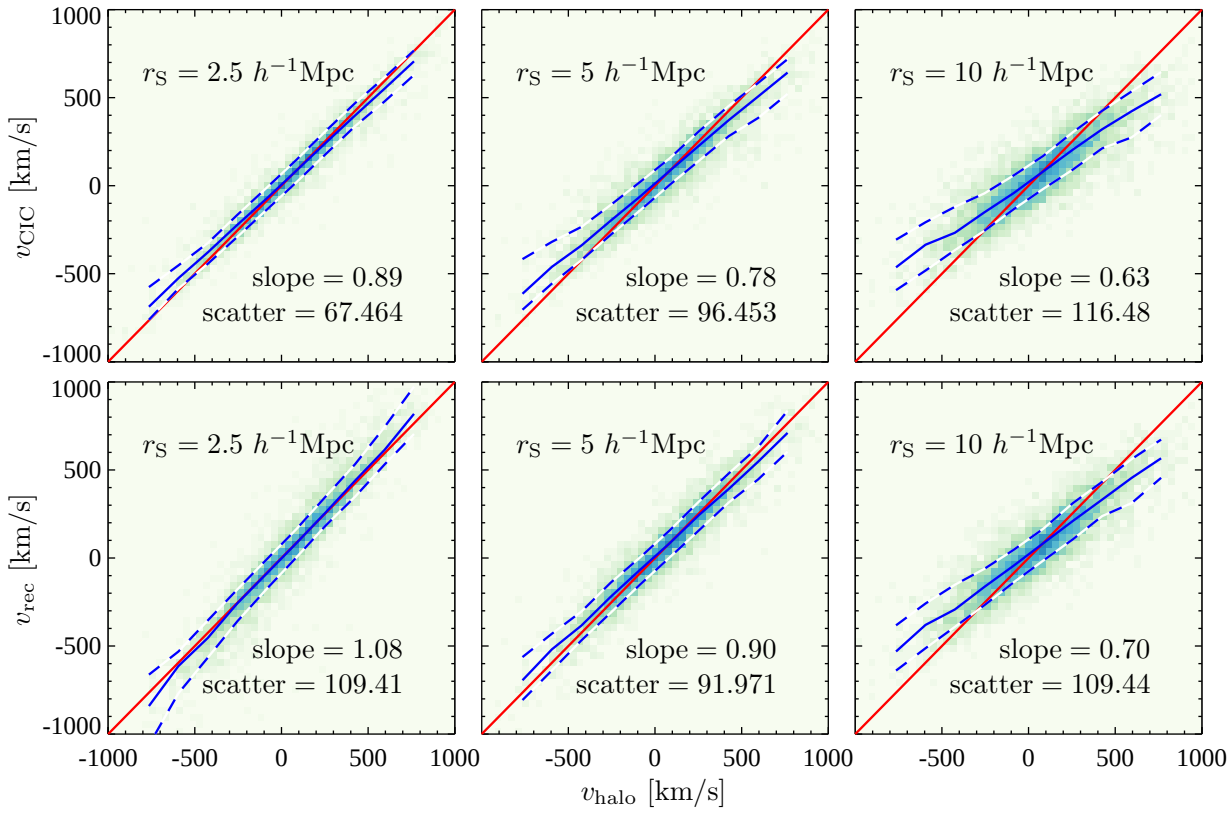

Figure 5. Top panels: one-to-one comparison between the true radial velocities of clusters $v_{\rm halo}$ and cluster velocities $v_{\rm CIC}$ from CIC assignment. Bottom panels: one-to-one comparison between the true radial velocities of clusters $v_{\rm halo}$ and cluster velocities $v_{\rm rec}$ from reconstruction method. The red solid line in each panel is the 1:1 line. The blue solid lines show the median relation binned by $v_{\rm halo}$. The dashed blue lines indicate the region containing the central 68 per cent scatter of the median relation. Left-hand panels on smooth scales of $2.5\,h^{-1}$Mpc, middle panels $5\,h^{-1}$Mpc and right-hand panels $10\,h^{-1}$Mpc.

turbation theory and (ii) how well a smoothed field approximates the actual velocity of the cluster. On small scales, we approximate better the velocity of cluster, however, linear theory breaks down overestimating the velocity field. On large scales, the performance of linear theory improves; however, the recovered smoothed velocity field underestimates the velocity at the clusters position. In other words, while the velocity field shows a high coherence, the velocity structure of regions as small as $2.5\,h^{-1}$Mpc can affect systematically high-precision measurements of the kSZ effect.

5.3.1 The systematics from velocity reconstruction

An additional source of uncertainty is introduced by the estimation of the DM density field from a distribution of galaxies. In particular, effects such as survey mask, selection function, shot noise, redshift space distortions will all add extra uncertainties in the recovered velocity field. One example of recovering a continuous and smooth 3D density field from a group of galaxies is presented in Jasche et al. (2010b), who applied a Hamiltonian density algorithm **HADES** to SDSS data (Release 7) and returned a set of 40000 possible realizations of the density field given the data and observational setup. An additional complication comes from the fact that we observe the galaxy field in redshift space, thus one needs to assume a value of β to estimate the corresponding velocity field. This, however, can be coupled with the kSZ measurements to sample different values of β in a self-consistent manner as we measure α.

The total error associated with the reconstructed velocity can be modelled as the sum of two independent terms

$$\sigma^2_{\rm rec} = \sigma^2_{\rm obs} + \sigma^2_{\rm meth}. \quad (22)$$

$\sigma_{\rm obs}$ refers to an uncertainty that depends on the particular observational setup propagated through the density reconstruction method. This term varies as a function of position and distance to the observer, and slightly depends on velocity. The second term, $\sigma_{\rm meth}$, is velocity-independent term and it accounts for the uncertainties in the method itself (i.e. the scatter shown in Fig. 5), which is around $100\ {\rm km\ s^{-1}}$.

In practice, it is difficult to estimate each of these two terms independently due to their correlation. However, the total error budget, $\sigma_{\rm rec}$, can be determined. As studied in Appendix A, a typical value of $\sigma_{\rm rec}$ is about $350\ {\rm km\ s^{-1}}$, for an SDSS-like survey. With more accurate reconstruction methods the uncertainty in $\sigma_{\rm meth}$ can be reduced to $20\ {\rm km\ s^{-1}}$ (Kitaura et al. 2012b). Therefore, $\sigma_{\rm rec}$

would be mainly determined by $\sigma_{\rm obs}$, which is position and distance dependent.

The value of $\sigma_{\rm rec}$ inferred above clearly indicates that the current limitation is in the quality of the data of a target galaxy survey, and the method to infer the DM density field. This turns into another issue that how well velocity reconstruction method could return the correct sign for each cluster. This would potentially affect the efficiency of our estimation on α. But with the aim to offer a clean forecast for our method, reconstruct velocities based on numerical simulation are used in this paper, without fully considering observational effects. We plan to further test the sign issue with more realistic data through the **HADES** pipeline in a forthcoming work.

In this paper, we just approximately account for the effect of $\sigma_{\rm rec}$, our Mock-MaxBCG clusters are assigned uncertainties in their line-of-sight velocity by interpolating the velocities and uncertainties reconstructed by **HADES** (shown in Appendix A) to the positions of our clusters. The total uncertainty can be incorporated in our approach by using the full form of the weights shown in equation (13).

We have repeated our analysis with this extra source of uncertainty. However, the estimated value of α remained almost identical to our previous case. This is because $\sigma_{\rm rec}$ plays a minor role in w_i compared to $\sigma_{\rm kSZ}$, which is dominated by the primary CMB fluctuations and instrumental noise and is at the level of a few thousands $\rm km\ s^{-1}$. Hence, the quality of the reconstructed velocity field does not affect significantly the estimated α, but mainly the α_i value for each clusters.

5.4 Cluster catalogue selection

A central part of our method is the existence of an appropriate cluster catalogue, and the accuracy of our method depends on its properties. Therefore, in this subsection and in Fig. 6 we explore how the selection criteria affect the accuracy with which we measure α. In particular, we consider different cuts in mass, in angular size and in redshift. For each threshold, we consider a simple case where we include only the CMB as a source of noise (top panel) and another in which we consider further sources of uncertainty (bottom panel). For clarity, we use the measured centre of mass velocity of each cluster. The results are shown in Fig. 6 and we discuss them next.

5.4.1 *Mass/Richness*

We recall that so far we have shown results for two different catalogues. (i) 'MXXL Selected', which contains all clusters in a SDSS-like volume with mass above $1.5 \times 10^{13} h^{-1}{\rm M}_\odot$, and (ii) 'Mock MaxBCG', which is a sub-sample of previous catalogue with a higher mass threshold $5 \times 10^{13} h^{-1}{\rm M}_\odot$. The latter corresponds to a threshold of optical richness $N_{200} = 10$ in the real MaxBCG catalogue. Systems above that richness are identified at high significance and suffer little contamination; however, below that limit there is still information about overdensities in the Universe. Thus, we explore whether these can increase the quality of our kSZ measurements.

In the leftmost panels of Fig. 6, we show the SNR as a function of the minimum cluster mass considered in the catalogue. The number of objects that this implies is displayed in the top axis. First, we note that the estimated value for α converges after roughly few thousands objects are included, noting that no difference between the Mock MaxBCG and the MXXL selected catalogues. Secondly, the SNR is roughly proportional to the number of clusters used, but the change is not as dramatic as one would have expected. There is a factor of 5 difference in the number of clusters among catalogues, so if we simply consider the number of systems, then one would have expected a reduction of a factor of $\sqrt{5} = 2.23$. The actual SNR improvement is about 25 per cent. This is because, the newly added systems will be much less massive, so their associated signal and angular extent on the sky are also smaller.

5.4.2 *Angular size*

We now consider the effect of varying the minimum angular size of clusters included in the catalogue. We show the results in the middle panels of Fig. 6 and, as in the previous case, top and bottom pales show two cases where we consider different sources of uncertainty. Black and blue lines indicate the results for the 'Mock BCG' and 'MXXL Selected' catalogues, respectively.

We see that the value for α quickly converges after we include objects with an apparent size of the sky larger than 10 arcmin. The SNR also increases rapidly as we include smaller and smaller objects; however, there is a clear saturation at $4 - 5$ arcmin, coinciding with the beam size in our simulated *Planck*-like CMB skies (5 arcmin). The plateau in the SNR seems to appear more smoothly in the bottom panel, which is because clusters comparable to, but larger than, the beam size are already being affected by the instrumental noise (which becomes dominant at around $\ell \sim 1600$). Nevertheless, it is important to note that the value of α is not affected and is largely insensitive to the threshold angular size we employ. This supports again the robustness of our approach.

Finally, the MXXL catalogue returns a higher SNR than the Mock MaxBCG, at all angular thresholds. Combining this information with that in the previous subsection, we see that the gain in SNR from reducing the threshold mass, largely originates from the small but nearby systems which are well resolved above the beam size.

5.4.3 *Redshift*

To end this section, in the rightmost panel of Fig. 6, we show the results we obtain as we vary the maximum redshift of clusters included in our analysis. We see that the bulk of the signal originates from clusters below redshift 0.2. This is partially because of the selection function applied to our catalogues, but mainly because high-redshift clusters have small angular extents, despite the enhanced volume covered. Finally, as expected, there is a roughly constant offset between the two cluster catalogues we consider, due to the higher number of objects in the MXXL selected catalogue, at all redshifts.

From this section, we can conclude that current cluster catalogues would capture almost all the signal available in a CMB experiment like *Planck*. Reducing the mass threshold does not increase significantly the SNR of the measurement because the extra systems will be less massive and thus contribute less to the total signal, and also because a considerable fraction of them will be below the beam size of the experiment. Moreover, the small systems usually have inaccurate measurement of cluster properties (richness, positions and so on), which may affect the definition of the matched filter and related signal. In the light of this, it seems that much more gain can be found in extending the sky coverage of survey within which the cluster population is well characterized rather than in employing lower mass systems.

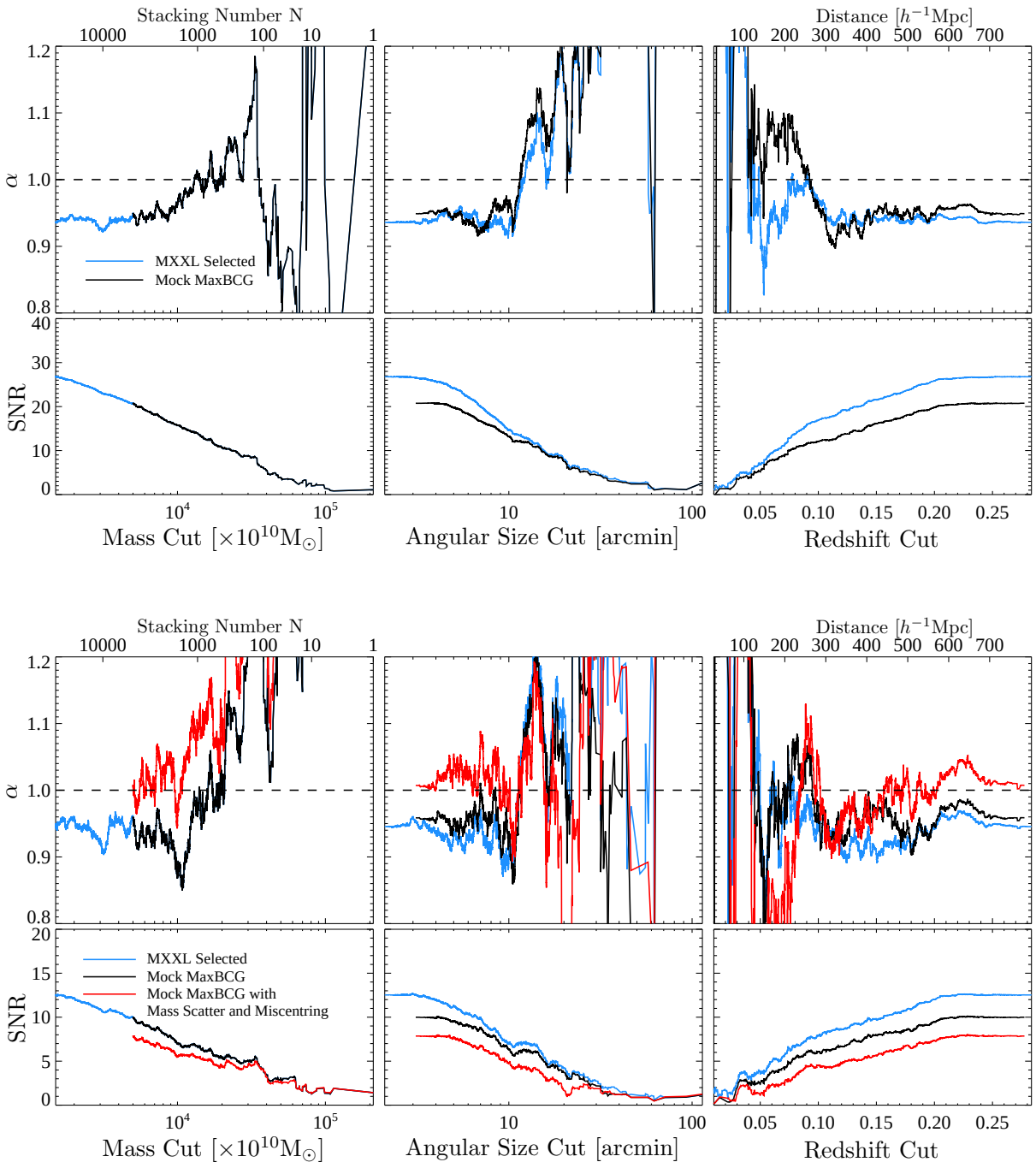

Figure 6. Top row set: top panels show the weighted estimation α (equation (11)) as a function of mass cut (left column), angular size cut (middle column) and redshift cut (right column) which are used to test cluster selection criteria from our catalogues. The corresponding stacked number is shown on top axis of mass cut case. Bottom panels show the corresponding SNR of α following the same way. The two cluster catalogues are used and shown as blue (MXXL selected) and black (Mock MaxBCG) curves. The analysis is based on map of kSZ+CMB and α using $v_{\rm halo}$ are shown as example. Bottom row set: the same as top row set plots, but α is analysed based on map of kSZ+CMB+Noise. Results of Mock MaxBCG when considering mass scatter and miscentring problems are also presented with red curves.

5.5 Summary of results

In this section, we have explored different sources of uncertainties in our proposed procedure. These findings are summarized in Fig. 7, where we plot our results grouped by the velocity estimation used and the respective smoothing scales. For each set, we show measurements progressively including four noise terms, as indicated by the legend. For each case filled squares show the results of a single measurement with error bars given by the matched filter formalism, whereas box plots show the median and the 1, 16, 84 and 99 percentiles of measurements over an ensemble of 50 realizations.

In the following, we summarize the most relevant findings:

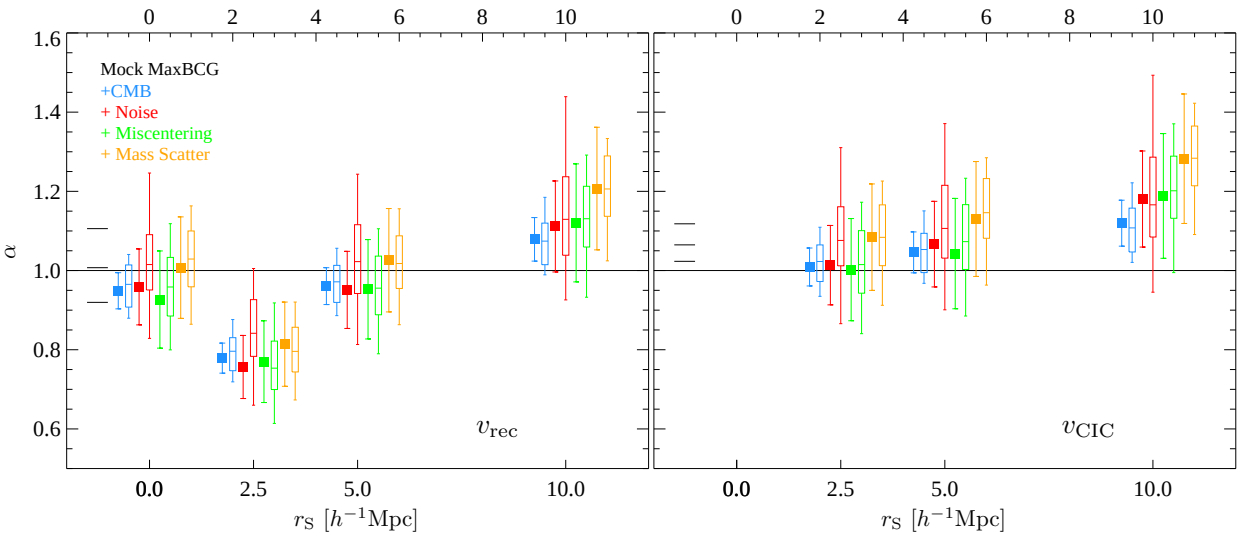

Figure 7. The measurement of α for Mock-MaxBCG clusters with different velocity references. Data sets are listed according to velocity used, $v_{\rm rec}$ (left-hand panel) and $v_{\rm CIC}$ (right-hand panel), their positions according to the smooth length $r_{\rm s}$. Specially measurement using $v_{\rm halo}$ is positioned in left-hand panel with x-axes $r_{\rm s} = 0$. For each set of data points, measurements with continuous including noise are distinguished with colours. The filled squares are single measurements, next to them are the corresponding measurement distributions estimated over 50 realizations. The bars, boxes and whiskers show the median and the 1, 16, 84 and 99 percentiles of the α distributions. The black solid lines at left-hand side of each panel present the bias level computed by taking median of $v_{\rm halo}/v_{\rm rec}$ or $v_{\rm halo}/v_{\rm CIC}$ at the three smoothing scales, from bottom to top 2.5, 5, 10 h^{-1}Mpc, respectively.

1) The main sources of statistical errors are: CMB primary fluctuations, instrumental noise, mass estimation, and cluster miscentring, each of which contributes about 13, 42, 5, and 40 per cent of the total error variance.

2) The main source of systematic errors is the estimation of velocity fields. There is a compromise between a smoothing scale small enough, such that it captures accurately the features of the velocity field, and a scale large enough such that perturbation theory is accurate. Additionally, if the miscentring is not properly accounted for, then there is a bias in the measurements of about 20 per cent.

3) Another potential source of systematic effect is from the mean mass–richness relation. If mass–richness relation provide a mass estimation biased by 10, 20, 40 per cent high (low), then α estimation will be biased 6, 10, 18 per cent low (6, 14, 34 per cent high), respectively.

4) Currently, the velocity field can be reconstructed to high accuracy using linear or higher order perturbation theory (Kitaura & Angulo 2012a). However, a source of uncertainty that remains dominant is the transformation from galaxy to DM overdensities.

5) A MaxBCG-like cluster catalogue includes most of the available signal. Smaller systems do not increase the SNR substantially, due to their small angular sizes and weak intrinsic signals. However, broader sky coverage would lead to a considerable gain in the SNR.

6) For a *Planck*-like experiment and a MaxBCG-like cluster catalogue, we forecast a 7.7σ measurement of the kSZ, assuming an estimate for the velocity field using linear theory and a $5\,h^{-1}$Mpc smoothing scale. Alternatively, this measurement can be interpreted as 13 per cent constraint on the value of β.

Despite the uncertainties related to the cluster catalogues, we have shown the potential that exists in the kSZ effect to measure cosmic velocity fields and thus to place constraints that complement those from other cosmological probes.

6 CONCLUSIONS

In this paper, we have proposed and investigated a scheme to measure the kSZ effect with relatively high signal-to-noise. The method combines the matched filter approach, an independent catalogue of clusters, and the velocity field predicted by perturbation theory applied to a galaxy redshift survey. The results can be used to explore the properties of ionized gas in clusters or to constrain the value of $\beta = f(\Omega_{\rm m})/b$. The latter, in turn, can be used to place constraints on the gravity law that connects the cosmic density and velocity fields.

We have shown the efficiency and accuracy of our approach by applying it to mock CMB maps, which contain a realistic kSZ signal as predicted by a large cosmological N-body simulation. Using a cluster catalogue similar to those extracted from the SDSS data, Planck-like CMB maps, and an estimate for the velocity field based on linear theory, we forecast a 7.7σ detection of the kSZ effect. This result includes the effect of several sources of uncertainty: primary CMB fluctuations, instrumental noise, mass scatter, and cluster miscentring. Each of these effects is responsible for 13, 42, 5, 40 per cent of the total error variance, respectively. In addition, we highlighted that if the potential miscentring of clusters is not taken into account properly, a bias of about 20 per cent is induced in the recovered signal. Similarly, if the scale on which the velocity field is reconstructed is too small, then perturbation theory is inaccurate, whereas if it is too large, then the features of the velocity field are not properly resolved. Unless corrected, both effects introduce systematic errors in kSZ estimates.

We also explored how the accuracy of our method depends on details of the cluster catalogue. For the cases we considered, the typical angular size of clusters corresponds to the scale on which

the effect of instrumental noise and beam size become important for a Planck-like CMB experiment. This implies that the kSZ signal of clusters with small angular sizes will be smeared out, reducing their contribution to the total accuracy of the detection. A similar effect is present when we varied the range of redshift and mass of clusters included in our catalogue. It appears that current cluster catalogues would capture most of the signal available, since lower mass systems do not significantly increase the SNR of the measurement. On the other hand, broader sky-coverage would lead to improved constraints.

Despite the realism of the mock skies adopted throughout this work, there are several effects which we have neglected. Most notable is the impact of hydrodynamical interactions on the kSZ signal. For instance, feedback from supermassive black holes at the centre of massive galaxies can alter the distribution of mass inside clusters and, potentially, even expel gas from the cluster altogether. However, these effects are still highly uncertain and it is unclear that they would be large enough to significantly alter the kSZ signal. Once understood, such effects could easily be incorporated in our formalism through a modified model for the signal profile. By dividing the kSZ measurements according to cluster mass, such systematic effects could be detected through an apparent dependence of the cosmological signal on cluster mass.

ACKNOWLEDGEMENT

ML thanks Carlos Hernández-Monteagudo, Stefan Hilbert, Jun Pan and Cheng Li for helpful discussions. SW and RA acknowledge support from ERC Advanced Grant 246797 “GALFORMOD”. JJ is partially supported by a Feodor Lynen Fellowship by the Alexander von Humboldt foundation and Benjamin Wandelt’s Chaire d’Excellence from the Agence Nationale de la Recherche. The authors would also like to thank the anonymous referee for helping improve this paper.

REFERENCES

Abazajian K. N., et al., 2009, ApJS, 182, 543
Angulo R. E., Springel V., White S. D. M., Jenkins A., Baugh C. M., Frenk C. S., 2012, MNRAS, 426, 2046
Angulo, R. E., Hahn O., Abel T., 2013, MNRAS, 434, 1756.
Biesiadzinski T., McMahon J., Miller C. J., Nord B., Shaw L., 2012, ApJ, 757, 1
Boylan-Kolchin M., Springel V., White S. D. M., Jenkins A., Lemson G., 2009, MNRAS, 398, 1150
Carlstrom J. E., et al., 2011, PASP, 123, 568
Dolag K., Sunyaev R., 2013, MNRAS, 432, 1600
Duffy A. R., Schaye J., Kay S. T., Dalla Vecchia C., 2008, MNRAS, 390, L64
Fowler J. W., et al., 2007, ApOpt, 46, 3444
Górski K. M., Hivon E., Banday A. J., Wandelt B. D., Hansen F. K., Reinecke M., Bartelmann M., 2005, ApJ, 622, 759
Haehnelt M. G., Tegmark M., 1996, MNRAS, 279, 545
Hand N., et al., 2012, PhRvL, 109, 041101
Hilbert S., White S. D. M., 2010, MNRAS, 404, 486
Ho S., Dedeo S., Spergel D., 2009, arXiv, arXiv:0903.2845
Jasche J., Kitaura F. S., 2010a, MNRAS, 407, 29
Jasche J., Kitaura F. S., Li C., Enßlin T. A., 2010b, MNRAS, 409, 355
Johnston D. E., et al., 2007, arXiv, arXiv:0709.1159
Kashlinsky A., Atrio-Barandela F., Ebeling H., Edge A., Kocevski D., 2010, ApJ, 712, L81
Kashlinsky A., Atrio-Barandela F., Ebeling H., 2011, ApJ, 732, 1
Keisler R., Schmidt F., 2013, ApJ, 765, L32
Kitaura F. S., Jasche J., Li C., Enßlin T. A., Metcalf R. B., Wandelt B. D., Lemson G., White S. D. M., 2009, MNRAS, 400, 183
Kitaura F.-S., Angulo R. E., 2012a, MNRAS, 425, 2443
Kitaura F.-S., Angulo R. E., Hoffman Y., Gottlöber S., 2012b, MNRAS, 425, 2422
Koester B. P., et al., 2007, ApJ, 660, 239
Lavaux G., Afshordi N., Hudson M. J., 2013, MNRAS, 430, 1617
Li M., et al., 2012, ApJ, 761, 151
Mak D. S. Y., Pierpaoli E., Osborne S. J., 2011, ApJ, 736, 116
Melin J.-B., Bartlett J. G., Delabrouille J., 2005, A&A, 429, 417
Melin J.-B., Bartlett J. G., Delabrouille J., 2006, A&A, 459, 341
Mody K., Hajian A., 2012, ApJ, 758, 4
Osborne S. J., Mak D. S. Y., Church S. E., Pierpaoli E., 2011, ApJ, 737, 98
Planck Collaboration, et al., 2014, A&A, 561, A97
Planck Collaboration, et al., 2013a, arXiv, arXiv:1303.5072
Planck Collaboration, et al., 2013b, arXiv, arXiv:1303.5081
Planck Collaboration, et al., 2013c, arXiv, arXiv:1303.5089
Rozo E., et al., 2009, ApJ, 699, 768
Schaffer K. K., et al., 2011, ApJ, 743, 90
Shao J., Zhang P., Lin W., Jing Y., Pan J., 2011, MNRAS, 413, 628
Springel V., et al., 2005, Natur, 435, 629
Sunyaev R. A., Zeldovich Y. B., 1972, CoASP, 4, 173
Sunyaev R. A., Zeldovich I. B., 1980a, MNRAS, 190, 413
Sunyaev R. A., Zeldovich I. B., 1980b, ARA&A, 18, 537
Swetz D. S., et al., 2011, ApJS, 194, 41

APPENDIX A: BEHAVIOUR OF VELOCITY UNCERTAINTIES WITH TRUE DATA AT POSITIONS OF MAXBCG CLUSTERS

In this work we use a sub-sample of 4000 density field realizations previously generated by the **HADES** (HAmiltonian Density Estimation and Sampling) algorithm (Jasche et al. 2010b). The **HADES** algorithm is a full scale Bayesian inference framework providing detailed reconstructions of the 3D density field from galaxy redshift surveys and corresponding uncertainty quantification by exploring a highly non-Gaussian and non-linear lognormal Poissonian posterior via efficient implementations of a Hybrid Monte Carlo method (Jasche & Kitaura 2010a). As a result, this algorithm provides a numerical representation of the target posterior distribution, in terms of density field realizations constrained by observations, permitting to thoroughly propagate uncertainties to any finally inferred quantity. In the following, we build upon the results obtained by Jasche et al. (2010b), which provide realizations of constrained density fields in a cubic Cartesian box of side length $547.5\,h^{-1}\mathrm{Mpc}$ and 256^3 voxels inferred from the SDSS DR7 main sample (Abazajian et al. 2009). The lower-left corner of the volume locates at $[-547.5, -273.75, -14.6]\,h^{-1}\mathrm{Mpc}$ and the observer is placed at $[0, 0, 0]$. To compute linear velocity fields, we smooth these density fields on length-scales of $5\,h^{-1}\mathrm{Mpc}$ and apply equation (8). Subsequently, we project the ensemble of resulting 3D velocity fields at each voxel on the observers line of sight. Given this ensemble, mean and standard deviation of radial velocities are calculated for each voxel.

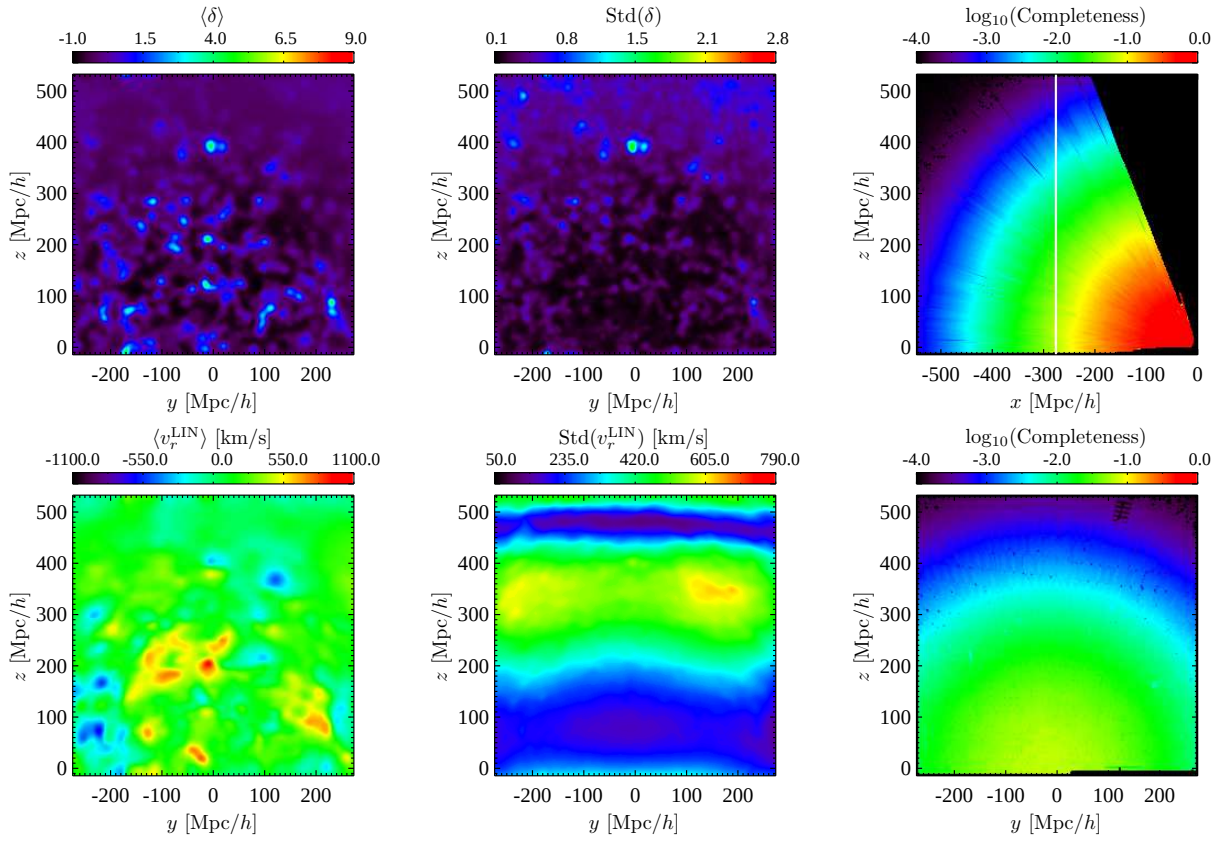

Figure A1. Slices for ensemble (4000 realizations) mean (left column) and standard deviation (middle column) of density contrast δ (top panels) and radial velocity $v_{\rm r}^{\rm LIN}$ (bottom panels). The right column shows a slice through the completeness function along y-axes and x-axes, respectively. The white solid line indicates the x-axes position of all other slices.

Results of these calculations as well as a slice through the corresponding completeness function of the underlying SDSS survey are presented in Figs. A1 and A2. As can be seen, close to the observer, structures are more clearly visible, while for poorly observed regions at large distances, the ensemble mean of the density contrast drops to cosmic mean. This reflects, the signal-to-noise properties of the underlying survey, as uncertainties increase with distance to the observer due to selection effects. This effect is clearly represented by the slices through estimated ensemble means and standard deviations as shown in Fig. A1. Slices through estimated ensemble means and standard deviations for radial velocities are presented in the bottom row of Fig. A1. For the mean velocity field, large speed regions coincide with high-density regions, being least affected by observational noise. On the contrary, ensemble standard deviation maps are more complicated to interpret. As can be seen, even at central regions where the observational completeness is at median level, ensemble standard deviations ranges around $400\ \mathrm{km\ s^{-1}}$. The reason for this may resort in the fact, that velocities, as estimated by equation (8), are most sensitive to the largest scales of the cosmic matter distributions, which are only poorly constrained by underlying galaxy observations, due to survey geometries. Observational uncertainties on these large scales are nevertheless correctly treated by the statistical nature of our approach. Additionally one may worry about periodic boundary conditions, assumed implicitly when estimating velocities via Fourier methods, which may influence the inference of velocities. This can be overcome by carrying out fast fourier transforms over a much larger volume, zero-padding the unobserved region.

The statistical study of the full volume is useful for the general analysis of the reconstruction method and the goodness of density fields. As a final step, we interpolate the reconstructed 3D velocities to positions of MaxBCG clusters (4044 clusters reside in our reconstruction volume) and estimate ensemble means and standard deviations of radial velocities. This addresses the issue of velocity uncertainties inherent to such reconstructions. We check the dependence of standard deviations on velocities and distances to the observer as demonstrated in Fig. A3. As can be seen, the standard deviation depends weakly on ensemble mean of $v_{\rm r}^{\rm LIN}$. Typically, the difference is less then $100\ \mathrm{km\ s^{-1}}$. The dependence on distance to the observer is essentially strong, and standard deviation peaks at around 480 and 780 $h^{-1}\mathrm{Mpc}$. The former peak shows the same complex behaviour as shown in Fig. A1. The latter one is mainly due to the fact of low completeness at such distances, and periodic boundary effects may also contribute. In general, velocity uncertainties are caused by the completeness function, indicating how much information the data provides. For the analysis in Section 5.3.1, we choose a constant velocity standard deviation to be $350\ \mathrm{km\ s^{-1}}$ for all clusters in our mock catalogue.

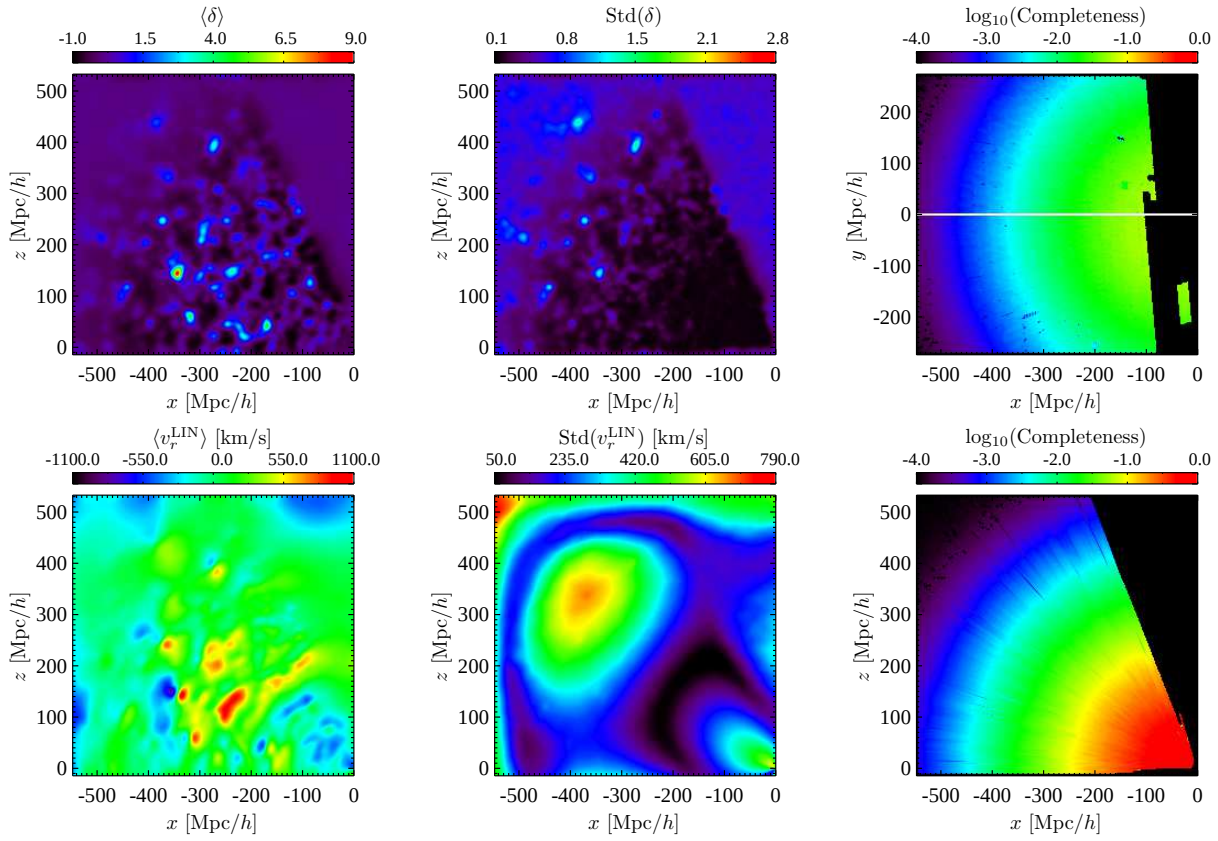

Figure A2. Same as Fig. A1 but density contrast δ (top panels) and radial velocity $v_{\rm r}^{\rm LIN}$ (bottom panels) are shown along the y-axes. The right column shows a slice through the completeness function along z-axes and y-axes, respectively. The white solid line indicates the y-axes position of all other slices.

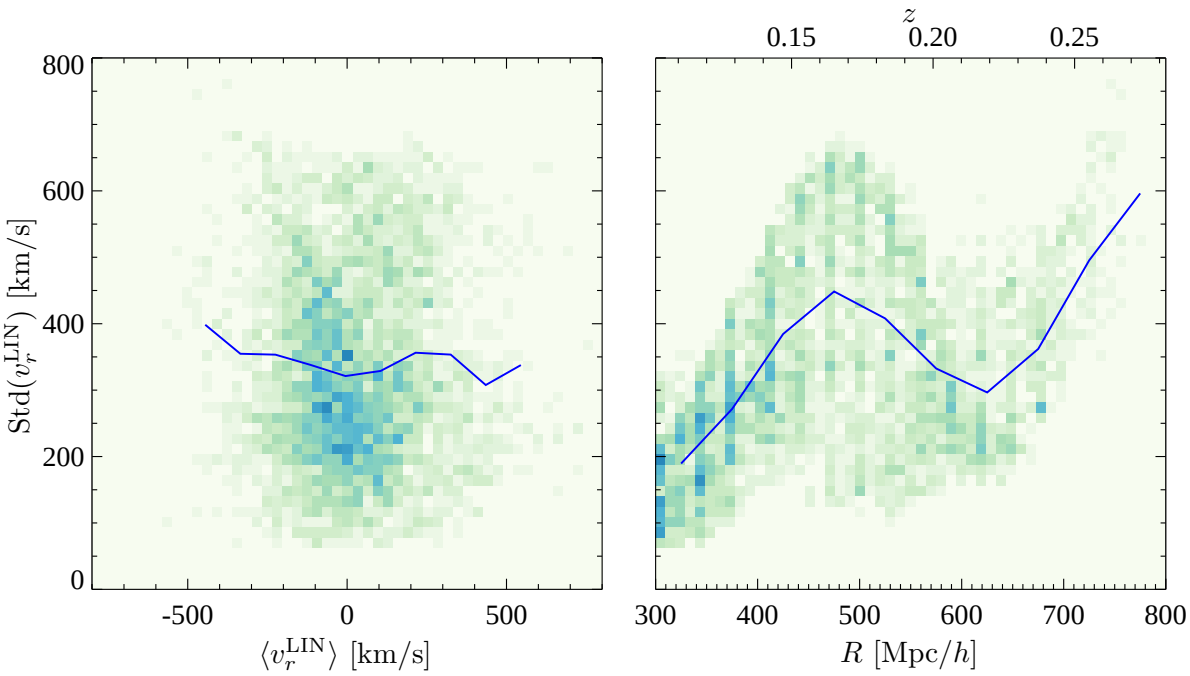

Figure A3. Ensemble (4000 realizations) standard deviation of radial velocities $\mathrm{Std}(v_{\mathrm{r}}^{\mathrm{LIN}})$ at positions of MaxBCG clusters as a function of their ensemble (4000 realizations) mean radial velocities $\langle v_{\mathrm{r}}^{\mathrm{LIN}} \rangle$ (left-hand panel) and radial distances to the observer R (right-hand panel). The intensity of background 2D histogram is proportional to the number of clusters that reside in corresponding region of the plot. The blue solid line is the mean relation binned by $\langle v_{\mathrm{r}}^{\mathrm{LIN}} \rangle$ and R.